DRAFT
CMS Paper

The content of this note is intended for CMS internal use and distribution only

2025/03/27
Archive Hash: e1f2550-D
Archive Date: 2025/03/27

Search for resonant production of pairs of dijet resonances through broad mediators in proton-proton collisions at $\sqrt{s} = 13$ TeV

The CMS Collaboration

Abstract

A reinterpretation of a prior narrow resonance search is performed to investigate resonant production of dijet resonance pairs via broad mediators. This analysis targets events with four resolved jets, requiring dijet invariant masses greater than 0.2 TeV and four-jet invariant masses greater than 1.6 TeV. The search uses a data sample corresponding to an integrated luminosity of 138 fb^{-1} collected by the CMS detector in proton-proton collisions at $\sqrt{s} = 13$ TeV. The reinterpretation considers the production of heavy new resonances with widths ranging from 1.5% to 10%, decaying to a pair of dijet resonances. This signature probes resonant production in the four-jet and dijet mass distributions. Both upper limits at 95% CL and significances are reported on the production cross section of new resonances as a function of their width and masses, between 2 and 10 TeV. In particular, for the 8 TeV four-jet mass region, where there was an excess in the previous narrow resonance search, the significance of an $8 - 10$ TeV diquark resonance is found to be relatively insensitive to the choice of width, making a broad resonance an equally valid interpretation of the excess. Also, we report the reinterpretation of a second effect, at a four-jet resonance mass of 3.6 TeV, which has a comparable local significance of up to 3.9 standard deviations.

This box is only visible in draft mode. Please make sure the values below make sense.

PDFAuthor:	CMS Collaboration
PDFTitle:	Search for resonant production of pairs of dijet resonances through broad mediators in proton-proton collisions at s = 13 TeV
PDFSubject:	CMS
PDFKeywords:	CMS, physics, paired dijets

Please also verify that the abstract does not use any user defined symbols

DRAFT

1 Introduction and motivation

Measurements of pairs of dijet resonances with the same invariant mass are powerful probes of new physics beyond the standard model (BSM). The pairs of dijet resonances can be produced resonantly via a massive s-channel mediator which can be wide.

Generic searches for resonant production of pairs of dijet resonances have recently been performed by the CMS [1] and ATLAS [2] collaborations. The data in both searches were used to constrain narrow mediators, with a natural width less than 0.5% of their mass, that is lower than the experimental resolution. Two events were observed in the CMS search with a four-jet mass of 8 TeV, and were interpreted as potential candidates for a narrow mediator, with a local significance of 3.9 standard deviations (s.d.) and a global significance of 1.6 s.d. The CMS and ATLAS searches did not conduct a wide resonance interpretation of their data. However, there were additional events observed by both CMS and ATLAS at high four-jet mass, and those events do compel us to search here for wide resonances decaying to pairs of dijet resonances.

We present a reinterpretation analysis of Ref. [1], searching now for resonant production of pairs of dijet resonances through broad mediators with data corresponding to an integrated luminosity of 138 fb^{-1} collected in 2016–2018 with the CMS detector at the LHC. Pairs of resolved dijet resonances, X, are considered, where both jets within each dijet resonance are individually reconstructed, allowing the search to be sensitive to high mediator masses: Y masses greater than 2.0 TeV.

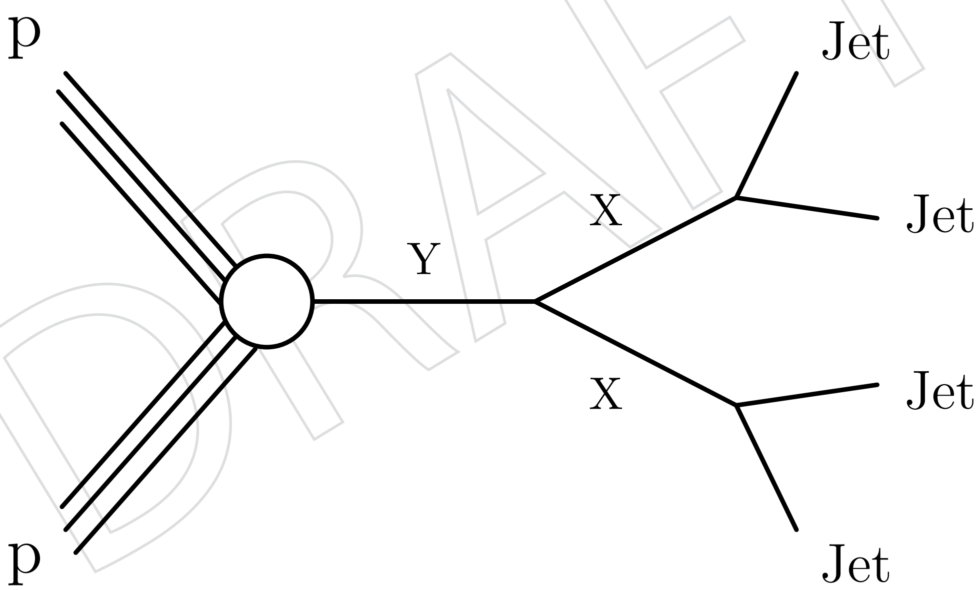

DRAFT

Figure 1: Resonant production via a particle, Y, of pairs of dijet resonances, X.

We consider resonant production of pairs of dijet resonances,

$$\mathrm{pp} \to \mathrm{Y} \to \mathrm{XX} \to (jj)(jj) \tag{1}$$

where the intermediate state is a massive new particle, Y, decaying to identical dijet resonances, X, as shown in Fig. 1. The natural width of particle Y is considered to be larger than the experimental resolution, thus forming a broad resonance, whereas particle X is characterized by a narrow intrinsic width. As a benchmark, we consider a diquark model [3], where the intermediate state is a diquark, S_{uu}, produced from the annihilation of two up quarks, and the dijet resonance is a vector-like quark, χ, that decays to an up quark (u) and a gluon (g).

$$\mathrm{uu} \to \mathrm{S_{uu}} \to \chi\chi \to (\mathrm{ug})(\mathrm{ug}) \tag{2}$$

This scalar diquark is a good benchmark because it is produced with a large cross section, due to the high probability of finding up quarks at high fractional momentum within the proton. Representatively, for an S_{uu} diquark with a mass of 8.4 (3.6) TeV and a width of 0.43% (10%), decaying to a vector-like quark with a mass of 2.1 (1.0) TeV, the cross section is 3.6×10^{-5} (2.3) pb.

Additionally, we consider and set mass exclusion limits on an extension of the aforementioned model, where a diquark S_{dd} is produced from the annihilation of two down quarks, and subsequently decays to a pair of vector-like quarks, ω, which in turn each decay to a down quark (d) and a gluon (g).

$$\mathrm{dd} \to \mathrm{S_{dd}} \to \omega\omega \to (\mathrm{dg})(\mathrm{dg}) \tag{3}$$

The Feynman diagrams of these models are shown in Fig. 2. The S_{uu} and S_{dd} are color sextet diquarks of charge 4/3 and -2/3, respectively. The branching fractions $\mathcal{B}(\mathrm{S_{uu}} \to \chi\chi)$ and $\mathcal{B}(\mathrm{S_{dd}} \to \omega\omega)$ are 0.63 when the vector-like quark mass to diquark mass ratio is 0.25. More generally, the branching fraction varies from 0.68 to 0.44 as the mass ratio increases from 0.11 to 0.42. We set $\mathcal{B}(\chi \to \mathrm{ug}) = 1$ and $\mathcal{B}(\omega \to \mathrm{dg}) = 1$, as is done in Ref. [3]. Throughout this paper the mass of both S_{uu} and S_{dd} is denoted by M_S.

The phenomenology of the diquark model and its implications for CMS searches with dijets has been explored in Refs. [3–5].

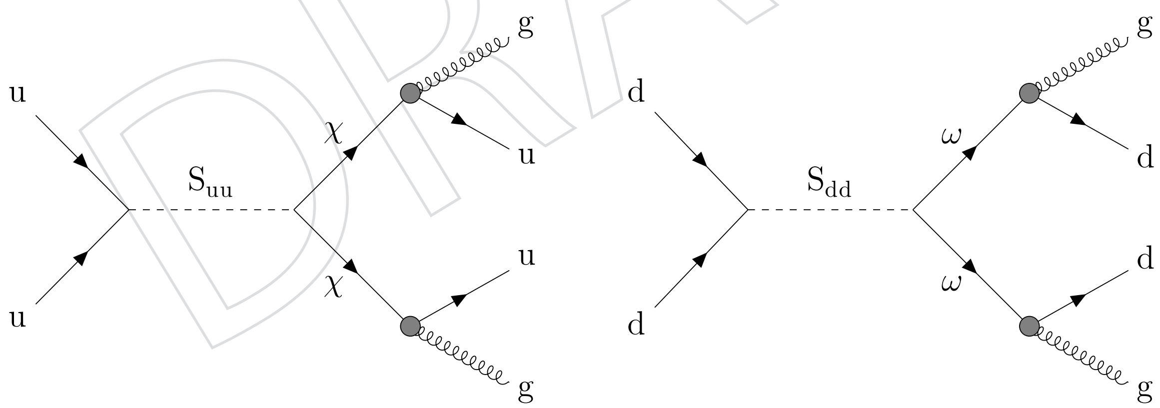

Figure 2: Diquark production followed by decay into a pair of vector-like quarks, each of them then decaying at one loop into a gluon and a quark.

This reinterpretation analysis is highly motivated by the data recorded from the CMS and ATLAS detectors, presented in Figs. 2 and 3a of Ref. [1] and [2] respectively. Besides the two events with a four-jet mass of 8 TeV, and average dijet mass of the two dijet pairs of 2 TeV, that were recorded in 2016–2018 by the CMS collaboration, an additional event with a four-jet mass of 5.8 TeV and average dijet mass of 2.0 TeV is found to be lying on top of the 90% probability contour of a narrow resonance with diquark mass of 8.4 TeV and χ mass of 2.1 TeV. Following this publication, the ATLAS experiment did not show an event with a four-jet mass of 8 TeV,

DRAFT

but presented an equally interesting event with a four-jet mass of 6.6 TeV and average mass of the two dijet pairs equal to 2.2 TeV, that also lies on top of the same contour. Hence, a broad resonance that would encompass these four candidate events in its 68% probability contour, may be a good fit to the combination of CMS and ATLAS datasets, which provides a strong physics motivation to extend the paired dijet search by exploring scenarios where the mediator Y is a broad resonance.

2 The CMS detector

A detailed description of the CMS detector and its coordinate system, including definitions of the azimuthal angle ϕ and pseudorapidity η, is given in Ref. [6]. The central feature of the CMS apparatus is a superconducting solenoid of 6 m internal diameter providing an axial magnetic field of 3.8 T. Within the solenoid volume are located the silicon pixel and strip tracker, and the barrel and endcap calorimeters ($|\eta| < 3.0$), where these latter detectors consist of a lead tungstate crystal electromagnetic calorimeter, and a brass and scintillator hadron calorimeter. An iron and quartz-fiber hadron calorimeter is located in the forward region ($3.0 < |\eta| < 5.0$), outside the solenoid volume. The muon detection system covers $|\eta| < 2.4$ with up to four layers of gas-ionization detectors installed outside the solenoid and embedded in the layers of the steel flux-return yoke.

3 Simulated data samples

A background sample of quantum chromodynamics (QCD) multijet events is produced, for the optimization of the search and qualitative comparisons with the observed data and the simulated signal datasets. The generation starts from the leading order (LO) QCD $2 \to 2$ processes of jet production, and includes additional jets from QCD initial- and final-state radiation within the parton shower. These background predictions are produced with the PYTHIA 8.205 Monte Carlo event generator, with the CUETP8M1 tune [7, 8], using the parton distribution function (PDF) set NNPDF2.3LO [9].

The benchmark model for the search is based on the aforementioned model of a diquark decaying to pairs of vector-like quarks, defined in Eq. (2). Specifically, we consider a scalar diquark resonance $\mathrm{S_{uu}}$ which decays to two vector-like quarks χ, which each then decay to a quark and gluon pair: $\mathrm{S_{uu}} \to \chi\chi \to (\mathrm{ug})(\mathrm{ug})$. The MADGRAPH5_aMC@NLO 2.6.5 [10] generator, with additional code specifying the model [3], is used to generate these events and MADSPIN is used for the vector-like quark decay to a quark and a gluon. Events for diquark masses between 2 and 10 TeV, for vector-like quark masses between 0.22 and 4.2 TeV and for diquark widths between 1.5% and 10% are generated. The same settings are utilized for the generation of events where an $\mathrm{S_{dd}}$ diquark decays to pairs of vector-like quarks, as defined in Eq. (3).

For the $\mathrm{S_{uu}}$ benchmark signal simulations, PYTHIA 8.205 [11] is used to produce the parton shower and the resulting final-state particles. The CP5 underlying event tune [7] is used with the NNPDF3.1NNLO PDF set [12], a next-to next-to leading order PDF.

The simulation of the CMS detector for all samples is handled by GEANT4 [13]. All samples include the effects of pileup and additional pp interactions in the same or adjacent bunch crossings. This pileup distribution in simulation is weighted to match the one observed in data.

DRAFT

4 Event reconstruction and selection

The event reconstruction and selection is identical to Ref. [1], given that the same data events are utilized, but for completeness they will be briefly described in this section.

A particle-flow (PF) event algorithm aims to reconstruct and identify each individual particle in an event, with an optimized combination of information from the various elements of the CMS detector [14]. Particles are classified as muons, electrons, photons, charged or neutral hadrons. To reconstruct jets from the input particles, the anti-k_{T} algorithm [15, 16] is used with a distance parameter of 0.4 as implemented in the FASTJET package [17]. The primary vertex (PV) is taken to be the vertex corresponding to the hardest scattering in the event, evaluated using tracking information alone, as described in Section 9.4.1 of Ref. [18]. Charged PF candidates not originating from the primary vertex are removed prior to the jet finding, as described in Ref. [19].

Events are selected using a two-tier trigger system [20, 21]. Events satisfying loose jet requirements at the first-level (L1) trigger are examined by the high-level trigger (HLT) system. At L1, single-jet triggers that require at least one jet in the event to exceed a predefined transverse momentum (p_{T}) threshold are used. Triggers that require H_{T} to exceed a threshold, where H_{T} is the scalar sum of jet p_{T} for all jets in the event with $p_{\mathrm{T}} > 30\,\mathrm{GeV}$ and $|\eta| < 3.0$, are also used. The HLT requires $H_{\mathrm{T}} > 1050\,\mathrm{GeV}$ or at least one jet reconstructed with an anti-k_{T} distance parameter of 0.8 and $p_{\mathrm{T}} > 550\,\mathrm{GeV}$.

The jet momenta and energies are corrected using calibration factors obtained from simulation, test beam results, and pp collision data at $\sqrt{s} = 13\,\mathrm{TeV}$. The methods described in Ref. [22] are used and all in-situ calibrations are obtained from the current data. Jets are required to have $p_{\mathrm{T}} > 80\,\mathrm{GeV}$ and $|\eta| < 2.5$. The four jets with the largest p_{T} are defined as the four leading jets. Jet identification criteria are applied to remove spurious jets associated with calorimeter noise, as well as those associated with muon and electron candidates that are either misreconstructed or isolated [23]. An event is rejected if any of the four leading jets fails these jet identification criteria.

As described in Ref. [1], the dijet pairs are constructed from the four leading jets utilizing a pairing algorithm that minimizes the quantity

$$\Delta R = |(\Delta R_1 - 0.8)| + |(\Delta R_2 - 0.8)| \tag{4}$$

where $\Delta R_{1,2}$ are the η-ϕ space separations between the jets in each dijet. This pairing algorithm was first used in the search for nonresonant production of pairs of dijet resonances [24]. It is motivated by the expectation that the jets from a dijet resonance will be closer together than uncorrelated jets, minimizing the separation of the jets, while the offsets of 0.8 reduce pairings where the jets overlap in η-ϕ space.

Once the jet pairing is complete, the same events as in Ref. [1] are selected that satisfy

$$\Delta R_{1,2} < 2.0 \tag{5}$$

These requirements reject background from hard multijet processes produced by QCD, which does not naturally give small separations in η-ϕ space between the jets in each dijet in a four-jet event. In addition, we require the η separation of the two dijets to satisfy

$$\Delta\eta = |\eta_1 - \eta_2| < 1.1 \tag{6}$$

which further suppresses background from QCD t-channel production compared to the signal from s-channel production. Finally, the asymmetry in dijet mass between the two dijets is required to be small,

$$\text{asymmetry} = \frac{|m_1 - m_2|}{m_1 + m_2} < 0.1 \tag{7}$$

selecting dijet pairs of approximately equal mass, a property of pairs of identical resonances, but not of the QCD background. Here, m_1 and m_2 denote the reconstructed mass of each dijet pair.

Throughout this paper, the small letter m denotes reconstructed dijet and four-jet masses, and the capital letter M denotes true resonance masses. Also, throughout this paper we will quote the resonance width as a percentage of the resonance mass, and denote it as the ratio of natural width (Γ) to resonance mass (M).

5 Analysis strategy

The resonant pair production, $\mathrm{Y} \to \mathrm{XX}$, produces a localized excess in both the four-jet invariant mass, $m_{4\mathrm{j}}$, and the average dijet invariant mass, $\overline{m}_{2\mathrm{j}}$, therefore these are the most natural variables to use for the search.

The plot on the left in Fig. 3 shows the 2D distribution of the observed data for $m_{4\mathrm{j}}$ vs. $\overline{m}_{2\mathrm{j}}$. At $m_{4\mathrm{j}} = 8\,\mathrm{TeV}$ and $\overline{m}_{2\mathrm{j}} = 2\,\mathrm{TeV}$ we observe two events, candidates for a narrow and broad resonant signal, as well as an additional event at $m_{4\mathrm{j}} = 5.8\,\mathrm{TeV}$ and $\overline{m}_{2\mathrm{j}} = 2.0\,\mathrm{TeV}$ that is more compatible with broad resonances. This is clearly illustrated in Fig. 3 from the colored solid lines that depict the 68% probability contours of the signal, from a simulation of our benchmark model of resonant pair production, for a diquark of mass 8.4 TeV and a vector-like quark mass of 2.1 TeV, with various widths ranging from 0.43% to 10%. Broad resonances of 5% and 10% width are better able to encapsulate all these three events than narrow resonances. The ATLAS event, with $m_{4\mathrm{j}}$ = 6.6 and $\overline{m}_{2\mathrm{j}}$ = 2.2 TeV, falls within the CMS 68% probability contour for a 5% or a 10% wide resonance with a mass of 8.4 TeV, and hence is compatible with those two hypotheses.

The challenge in evaluating the significance of this signal is to understand the background. Perturbative QCD predictions of multijet production have too many theoretical uncertainties to reliably model this background. We instead use an approach that does not rely on simulation, by fitting a smooth background parameterization function to the observed data. We do this with a set of 1D distributions that span the 2D space.

The background modelling has already been presented in Ref. [1]. Due to correlations between $m_{4\mathrm{j}}$ and $\overline{m}_{2\mathrm{j}}$, apparent in the left plot of Fig. 3, that would introduce sculpting of their distributions, we define a new variable $\alpha = \overline{m}_{2\mathrm{j}}/m_{4\mathrm{j}}$, which is the ratio of the two defined variables and a measure of the boost of the two dijet systems, and bin the 2D data in slices of this variable, constructing unbiased 1D $m_{4\mathrm{j}}$ distributions, as can be seen on the right in Fig. 3. The lowest α value we consider is 0.1 with a bin width of 0.02, which is comparable to the reconstructed α resolution, up to an α of 0.34, and then we utilize an overflow bin for all higher α values. The optimization of this binning has been performed in Ref. [1].

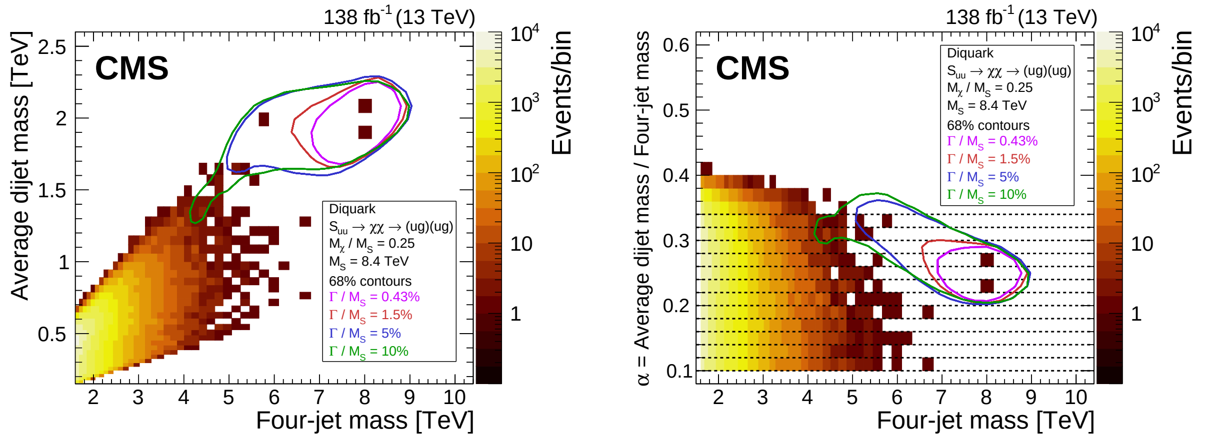

Figure 3: Numbers of events observed (color scale) within bins of the four-jet mass and the average mass of the two dijets (left) and within bins of the four-jet mass and the ratio α (right), which is the average dijet mass divided by the four-jet mass. The solid curves show the 68% probability contours from a signal simulation of a diquark with a mass of 8.4 TeV, decaying to a pair of vector-like quarks, each with a mass of 2.1 TeV. The violet, red, blue and green probability contours correspond to 0.43%, 1.5%, 5% and 10% diquark widths, respectively. The right plot also shows the thirteen α bins used to define the four-jet mass distributions (dashed lines).

Figure 4 shows the 2D distribution of the number of events predicted from a QCD simulated dataset, as a function of $\overline{m}_{2j}$ and m_{4j} (left), and α and m_{4j} (right). Events originating from QCD processes are distributed with an approximately uniform density in α, and for each value of α there is a wide unbiased range of m_{4j} to facilitate estimation of the background in data. Resonant signals, on the other hand, are observed as localized excesses in this 2D plane, as can be seen from the 68% probability contours of narrow and broad resonances with a diquark mass of 8.4 TeV, depicted in Fig. 4.

As in Ref. [1], the search is performed for four-jet masses $m_{4j} > 1.6$ TeV for all α values, for which the trigger is found to be fully efficient.

DRAFT

6 Signal simulations

The natural width, Γ/M_S, of a diquark S_{uu} is calculated from the sum of the partial width of its decay into a pair of up quarks,

$$\frac{\Gamma(S_{uu} \rightarrow uu)}{M_S} = \frac{y_{uu}^2}{32\pi} \tag{8}$$

and the partial width of its decay into a pair of vector-like quarks,

$$\frac{\Gamma(S_{uu} \rightarrow \chi\chi)}{M_S} = \frac{y_\chi^2}{32\pi}(1 - 2\alpha_{true}^2)(1 - 4\alpha_{true}^2)^{1/2} \tag{9}$$

where $\alpha_{true} = M_\chi/M_S$, y_{uu} (y_χ) is the coupling between the diquark and up quarks (vector-like quarks), as defined in Ref. [3], and the benchmark value of $\beta = y_{uu}/y_\chi$ is set to 2/3 as in Ref. [1]. For each α_{true} signal scenario the couplings y_{uu} and y_χ are chosen accordingly so as

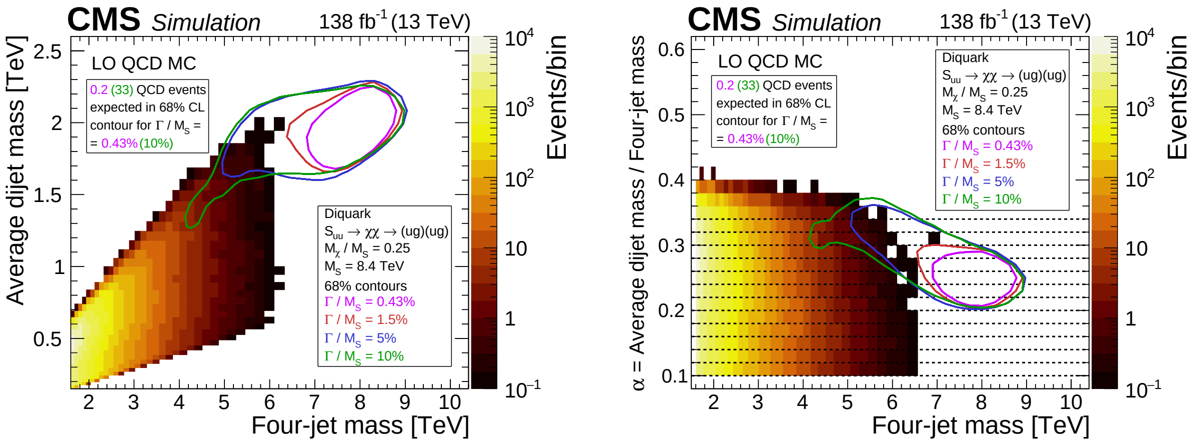

Figure 4: Numbers of events (color scale) within bins of the four-jet mass and the average mass of the two dijets (left) and within bins of the four-jet mass and the ratio α (right), which is the average dijet mass divided by the four-jet mass, predicted by a LO QCD simulation, normalized to the luminosity of data. Superimposed with solid lines are the 68% probability contours of narrow and broad diquark resonances with mass of 8.4 TeV, $M_\chi / M_S = 0.25$ and widths ranging from 0.43% to 10%. The right plot also shows the thirteen α bins used to define the four-jet mass distributions (dashed lines). The number of SM events, predicted by the LO QCD simulation, enclosed within the 68% probability contours of signals with 0.43% and 10% widths are 0.2 and 33 respectively.

to generate resonances with a total natural width of 1.5%, 5% and 10%, while keeping β at its benchmark value $\beta = 2/3$. Diquark signals with a width larger than 10% are too broad, they do not exhibit a peak at the resonance mass, and hence they are outside the scope of this analysis.

Figure 5 shows the shapes of signals with $\alpha_{\text{true}} = 0.25$ and various S_{uu} masses, across all α bins. Broad resonances with a natural width of 1.5%, 5% and 10% are furthermore compared with narrow resonances, presented in Ref. [1], where $y_{uu} = 0.4$ and $y_\chi = 0.6$ were set, yielding a width of 0.43%. Low-mass resonances exhibit a shift toward higher four-jet masses as their natural width increases, whereas intermediate-mass resonances display a broader distribution extending to both lower and higher four-jet masses. Conversely, high-mass resonances present a long, low-mass tail that becomes increasingly prominent with greater natural width, resulting in an improved description of both the two events observed near 8 TeV, and the CMS and ATLAS events with a four-jet mass of 5.8 and 6.6 TeV respectively.

The products of acceptance and efficiency are shown in Fig. 6 for all widths considered, as a function of diquark mass. The acceptance is defined as the fraction of events passing the kinematic selection criteria. The efficiency is the fraction of signal events satisfying the four-jet mass threshold previously discussed. Figure 6 also shows the signal acceptance alone, the curves where the efficiency is equal to 1. Cross section upper limits in this paper are quoted within this acceptance and corrected for efficiency. A decrease in the acceptance at the very highest values of signal mass, that is enhanced as the diquark width increases, is observed, and is found to originate from the mass asymmetry and ΔR requirements.

7 Background estimation

The background in this search is derived exclusively from data, and the procedure to estimate it is identical to that used in the narrow resonance search, presented in Ref. [1]. As in pre-

DRAFT

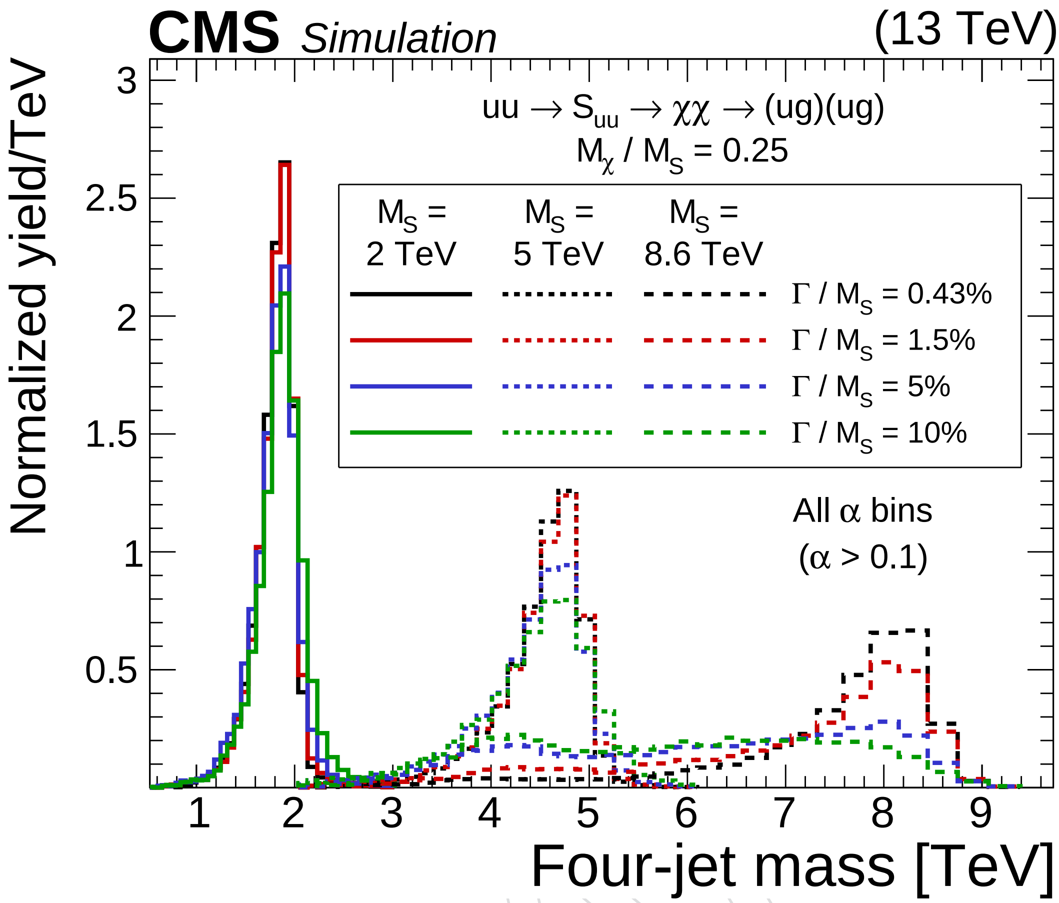

Figure 5: Signal differential distributions as a function of four-jet mass for $\alpha_{\mathrm{true}} = 0.25$, diquark masses of 2, 5, 8.6 TeV and various widths, for all α bins inclusively. The integral of each distribution has been normalized to unity.

vious resonance searches [25–40], we fit empirical functional forms to the observed multijet mass distributions. Our primary background function, which gives the best fit to the differential cross section data without including any signal component, is the modified dijet function (`ModDijet-3p`) given by

$$\frac{\mathrm{d}\sigma}{\mathrm{d}m_{4\mathrm{j}}} = \frac{p_0(1-x^{1/3})^{p_1}}{x^{p_2}} \tag{10}$$

where p_0, p_1, p_2 are free parameters and $x = m_{4\mathrm{j}}/\sqrt{s}$. We use two alternate background functions to estimate the systematic uncertainty in the background from variations in the functional form: the dijet function (`Dijet-3p`) given by

$$\frac{\mathrm{d}\sigma}{\mathrm{d}m_{4\mathrm{j}}} = \frac{p_0(1-x)^{p_1}}{x^{p_2}} \tag{11}$$

and the power-law times exponential function (`PowExp-3p`) given by

$$\frac{\mathrm{d}\sigma}{\mathrm{d}m_{4\mathrm{j}}} = \frac{p_0 e^{-p_2 x}}{x^{p_1}} \tag{12}$$

DRAFT

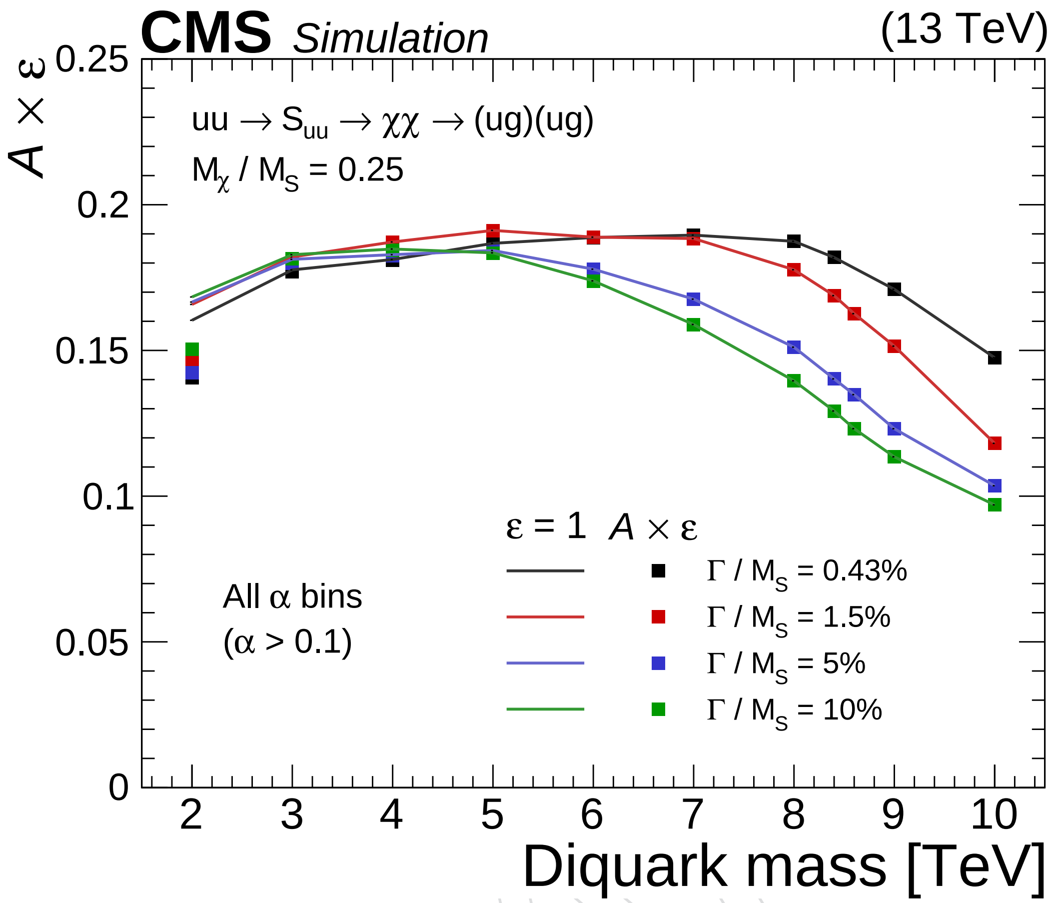

Figure 6: The product of acceptance and efficiency (squares) of a resonant signal with $\alpha_{\mathrm{true}} = 0.25$ vs. the diquark mass for various diquark widths, and for all α bins inclusively. The case when the efficiency of the mass selection is unity is also shown as solid lines.

Figure 7 shows the three functional forms, fitted to examples of the observed differential cross section, as functions of four-jet mass, and the simulation of the QCD background, for six out of the thirteen α bins that contain 90% (80%) of a narrow (broad) signal with $M_S = 8.6$ TeV and $\alpha_{\mathrm{true}} = 0.25$. Figure 8 demonstrates similar distributions for three α bins that contain 80% (70%) of a narrow (broad) signal with $M_S = 3.6$ TeV and $\alpha_{\mathrm{true}} = 0.29$. In Section 8 we will present more information on both these signals.

The candidate event for a broad resonance, with a four-jet mass of 5.8 TeV and average dijet mass of 2.0 TeV, is the highest mass event in the $0.32 < \alpha < 0.34$ bin in Fig. 7. This event is described in more detail in Section 9. For the highest mass signal of interest, with $\alpha_{\mathrm{true}} = 0.25$ and $M_S = 8.6$ TeV, if the width is 10% then the $0.32 < \alpha < 0.34$ bin contains roughly 10% of the signal, compared to only 2% for a narrow resonance of the same mass. Consequently, such a broad resonance is potentially able to provide a suitable fit for the three highest m_{4j} and $\overline{m}_{2j}$ events observed. A broad resonance includes the tail event at four-jet mass of 5.8 TeV in the $0.32 < \alpha < 0.34$ bin and additionally preserves the main peak at roughly 8 TeV in the $0.22 < \alpha < 0.24$ and $0.26 < \alpha < 0.28$ bins.

To better visualize how the broadest resonance considered more effectively encapsulates the three candidate events simultaneously, the inclusive four-jet mass distribution corresponding to the sum of all thirteen α bins is shown in Fig. 9, alongside the inclusive signal shapes. Superimposed in Fig. 9, are also the background-only fits that are performed using the same func-

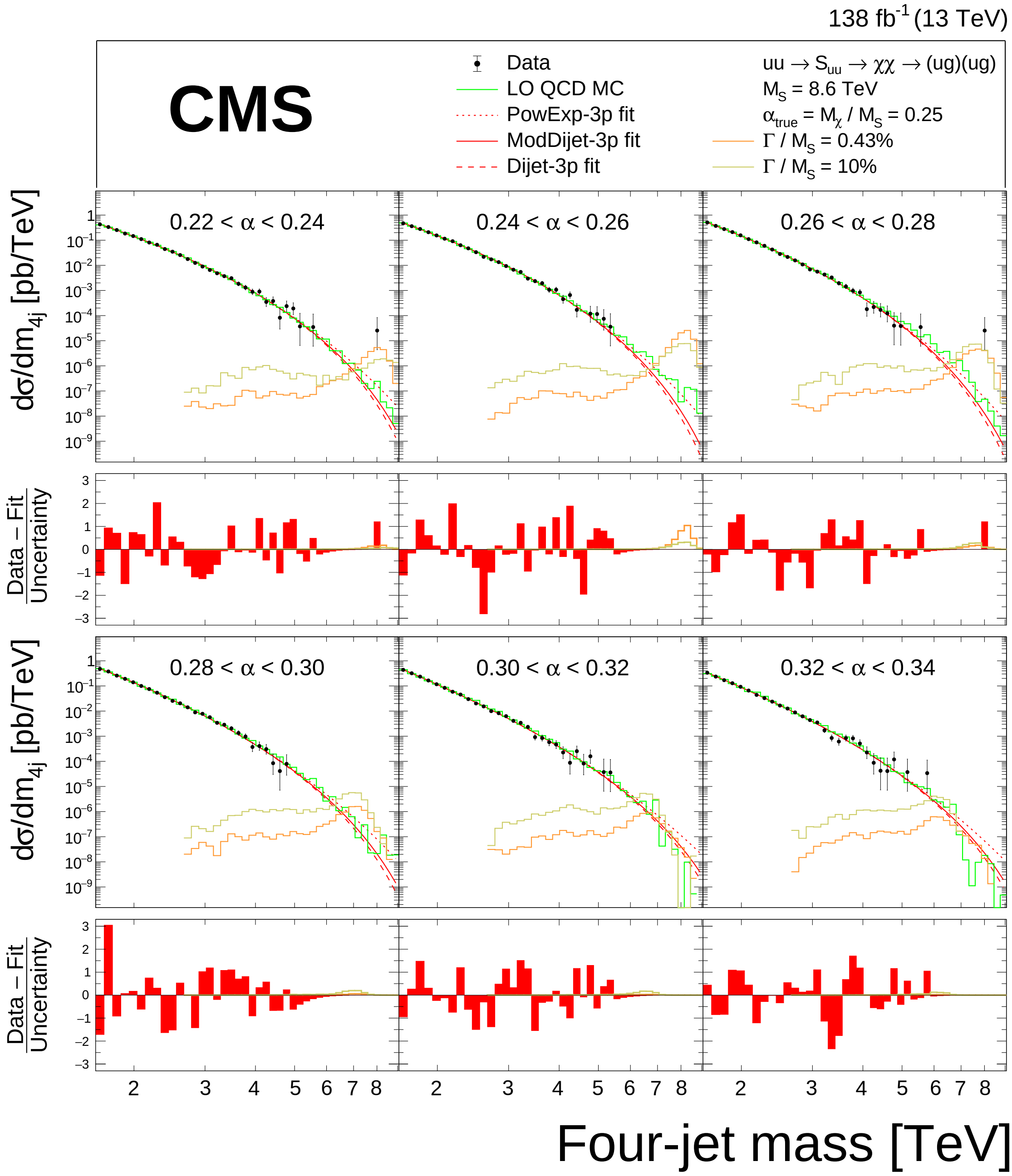

Figure 7: The four-jet mass distributions of the data (points), within six of the thirteen α bins, compared with the simulated LO QCD background distribution (green histogram) and fitted with three functions: a power-law times an exponential (red dotted), the dijet function (red dashed), and the modified dijet function (red solid), each function with three free parameters. Examples of predicted narrow (0.43%) and broad (10%) diquark resonances with $\alpha_{\text{true}} = 0.25$ and $M_S = 8.6$ TeV are shown, with cross sections equal to the observed upper limits at 95% confidence level. The percentage of signal across the depicted α bins is 90% (80%) for the narrow (broad) resonance. The lower panels show the pulls from the fit of the modified dijet function to the data, calculated using the statistical uncertainty of the data.

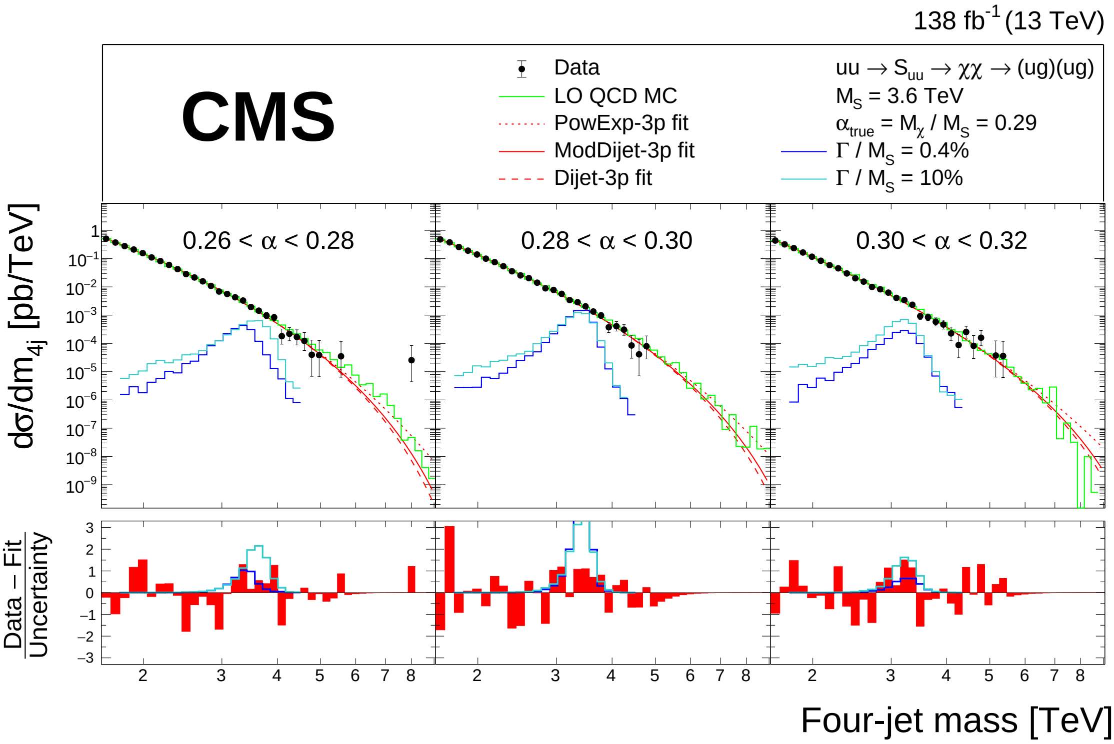

Figure 8: The four-jet mass distributions of the data (points), within three of the thirteen α bins, compared with the simulated LO QCD background distribution (green histogram) and fitted with three functions: a power-law times an exponential (red dotted), the dijet function (red dashed), and the modified dijet function (red solid), each function with three free parameters. Examples of predicted narrow (0.4%) and broad (10%) diquark resonances with $\alpha_{\text{true}} = 0.29$ and $M_S = 3.6$ TeV are shown, with cross sections equal to the observed upper limits at 95% confidence level. The percentage of signal across the depicted α bins is 80% (70%) for the narrow (broad) resonance. The lower panels show the pulls from the fit of the modified dijet function to the data, calculated using the statistical uncertainty of the data.

tional forms, but with five parameters due to the larger event samples. These are the modified dijet function (`ModDijet-5p`) given by

$$\frac{\mathrm{d}\sigma}{\mathrm{d}m_{4\mathrm{j}}} = \frac{p_0(1-x^{1/3})^{p_1}}{x^{p_2+p_3\log x+p_4\log^2 x}} \tag{13}$$

the dijet function (`Dijet-5p`) given by

$$\frac{\mathrm{d}\sigma}{\mathrm{d}m_{4\mathrm{j}}} = \frac{p_0(1-x)^{p_1}}{x^{p_2+p_3\log x+p_4\log^2 x}} \tag{14}$$

and the power-law times exponential function (`PowExp-5p`) given by

$$\frac{\mathrm{d}\sigma}{\mathrm{d}m_{4\mathrm{j}}} = \frac{p_0 e^{-p_2 x - p_3 x^2 - p_4 x^3}}{x^{p_1}} \tag{15}$$

where $x = m_{4\mathrm{j}}/\sqrt{s}$.

As demonstrated in Ref. [1], all the fits in each α bin adequately describe the data, with individual p-value ranging from 0.14 to 0.91. The combined p-value is 0.18 for a simultaneous fit of the data with the background function, including all thirteen α bins. This came from conducting a goodness-of-fit test on pseudo-experiments, utilizing a binned likelihood ratio with respect to the saturated model as the test statistic. This probability, and the pulls of the individual fits, indicate that the background model gives a good description of the data overall.

8 Results

The search uses a fit of the background function plus the simulated signal shape to the data, taking into account statistical and systematic uncertainties. As discussed, the data are the four-jet mass distributions in thirteen bins of α, and the fit is done simultaneously for all these bins. The results of the search are the expected and observed upper limits on the product of the signal cross section, branching fraction, and acceptance for all experimentally accessible values of resonance mass and width.

The dominant sources of systematic uncertainty in the signal modeling are the jet energy scale, the jet energy resolution, and the integrated luminosity. This analysis, as all previously published dijet or paired dijet ones, does not consider theoretical uncertainties on the signal shape or cross section, such as uncertainties in PDFs, parton showering, higher orders of calculation, or interference effects with the QCD background. They are model dependent and significantly complicate the analysis. Such uncertainties are deemed inappropriate for this model-independent search, and are not needed for mass limits on recently introduced benchmark models with arbitrary coupling values. The uncertainties with the largest impact on the extracted signal yield are the ones relating to background, with the signal modeling related ones being negligible. The uncertainty in the jet energy scale is below 2% for all values of the four-jet mass and is propagated to the limits by shifting the four-jet mass shapes for the signals by $\pm 2\%$. The uncertainty in the jet energy resolution translates into an uncertainty of 10% in the resolution of the four-jet mass [22], and is propagated to the limits by observing the effect of increasing the reconstructed width of the four-jet mass shapes for the signals by 10%. The total integrated luminosity has an uncertainty of 1.6%, the improvement in precision relative to

DRAFT

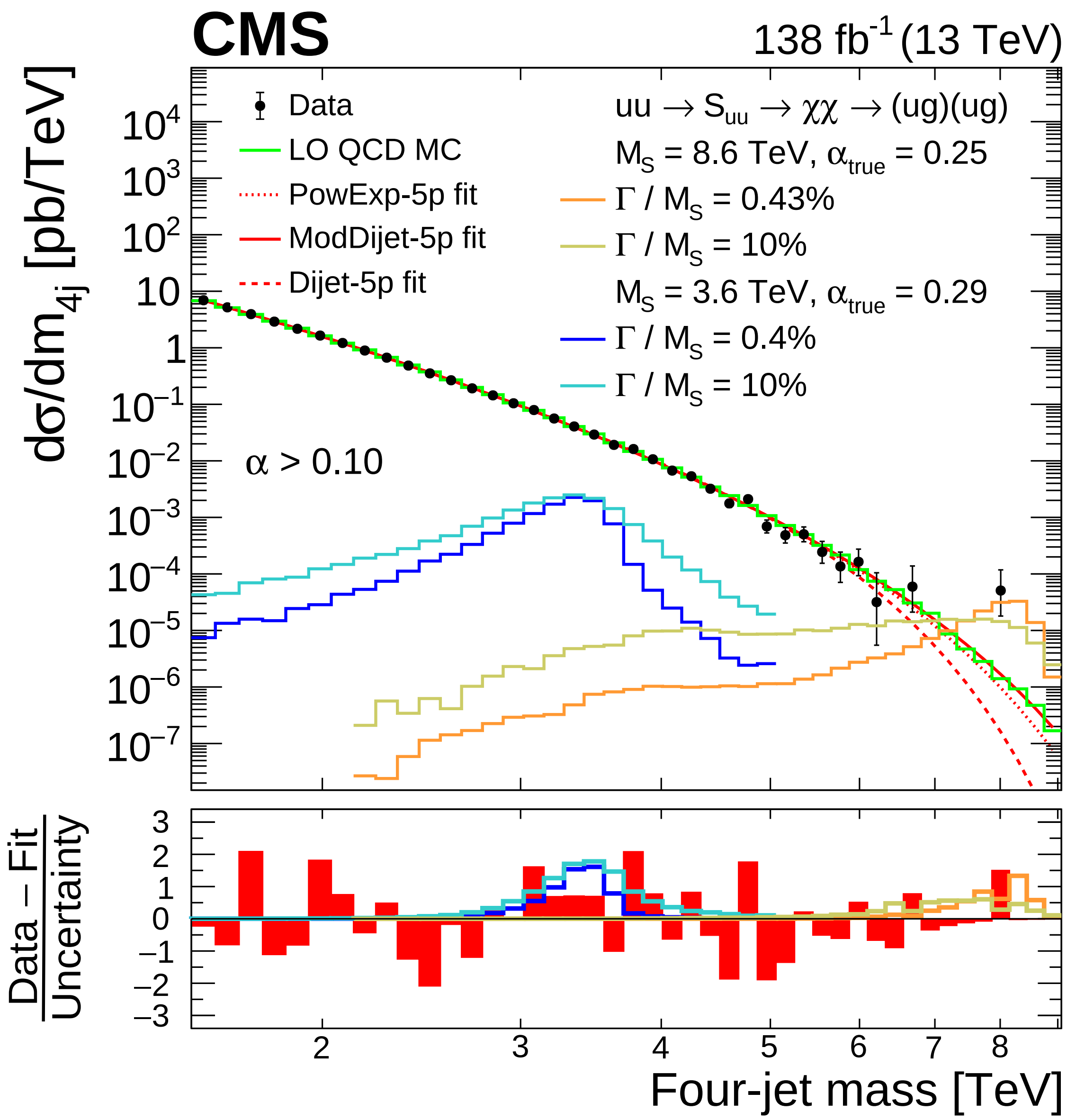

Figure 9: The four-jet mass distribution of the data (points), for all α bins combined, compared with the simulated LO QCD background distribution (green histogram) and fitted with three functions: a power-law times an exponential (red dotted), the dijet function (red dashed), and the modified dijet function (red solid), each function with five free parameters. Examples of predicted narrow (0.4%) and broad (10%) diquark resonances with $\alpha_{\mathrm{true}} = 0.25$, $M_{\mathrm{S}} = 8.6$ TeV and $\alpha_{\mathrm{true}} = 0.29$, $M_{\mathrm{S}} = 3.6$ TeV are shown, with cross sections equal to the observed upper limits at 95% confidence level. The lower panel shows the pulls from the fit of the modified dijet function to the data, calculated using the statistical uncertainty of the data.

Refs. [41–43] reflects the uncorrelated time evolution of some systematic effects, and is propagated to the normalization of the signal. Changes in the background function used, and the values of the background function parameters as estimated from the fit, can introduce changes in the signal yield. All these systematic uncertainties are included in the extracted cross section, limits and significance, as discussed in the next paragraph.

For the signal extraction, we use a multibin counting-experiment likelihood, which is a product of Poisson distributions corresponding to different bins. We evaluate the likelihood independently at each value of Y resonance mass from 2 to 10 TeV in 0.1 TeV steps and at each value of Y width: 1.5%, 5% and 10%. The step sizes in resonance mass are comparable to the experimental mass resolution at the lower edge of each resonance mass interval. The sources of systematic uncertainty are implemented as nuisance parameters in the likelihood model, with Gaussian constraints for the jet energy scale and resolution, and log-normal constraints for the integrated luminosity. The main source of the uncertainty in the background modeling comes from the choice of the background function, and the range of possible values of the parameters of the background function. The parameters of the empirical functional form used to describe the background are considered as freely floating nuisances, and are evaluated via profiling. The discrete profiling method [44] is used for considering the choice of the functional form as a discrete nuisance parameter, which is profiled in an analogous way to continuous nuisance parameters.

Next, we proceed in setting limits, and estimating significances, utilizing the COMBINE statistical package [45]. The modified frequentist criterion [46, 47] is used to set upper limits on the signal cross sections, following the prescription described in Refs. [48, 49], using the asymptotic approximation of the test statistic. In cases where the small number of events would make this approximation less accurate, the limit and significance estimation with respect to the background-only hypothesis is performed using test-statistic distributions derived from pseudo-experiments.

Limits from this procedure are presented in Figs. 10–12. First we show in Fig. 10 limits for the four widths considered, for signals with $\alpha_{\mathrm{true}} = 0.25$, the value of α_{true} where maximum significance is achieved in the $8 - 10$ TeV resonance mass range. Figure 10 presents the model-independent observed and expected upper limits at 95% confidence level (CL) on $\sigma\mathcal{B}A$, representing the product of the cross section (σ), the branching fraction ($\mathcal{B}$), and the acceptance (A) for the kinematic requirements. In Fig. 10 the observed limit is greater than the expected limit at resonance masses of around 2, 4 and 8 TeV, and less than the expected limit near a resonance mass of 3 TeV, due to similar effects in the pulls near these values of four-jet mass in Fig. 9. Furthermore, for the largest width considered in the analysis, Fig. 11 shows the observed and expected limits on resonant production for twelve values of α_{true}, chosen at the center of each bin of α. In Fig. 12 the observed limits are shown for all all α_{true} values and are superimposed for each width considered.

All upper limits presented can be compared to the predictions of $\sigma\mathcal{B}A$ to determine mass limits on new particles. In Figs. 10–12 we compare these limits to the predicted cross section times branching fraction for the scalar $\mathrm{S_{uu}}$ and $\mathrm{S_{dd}}$ diquark models, multiplied by the acceptance in Fig. 6. For the prediction we use a leading order (LO), MADGRAPH5_aMC@NLO calculation with NNPDF NNLO 3.1 PDFs. The cross section from this prediction is found to scale more rapidly than width at large resonance masses, due to the dominance of the long, low-mass tails. Since these do not contribute to the signal search, as they lie in a region that is dominated by background, we adjust the cross section from the theoretical prediction using an efficiency factor that isolates the four-jet mass range where the expected significance exceeds 99% of that

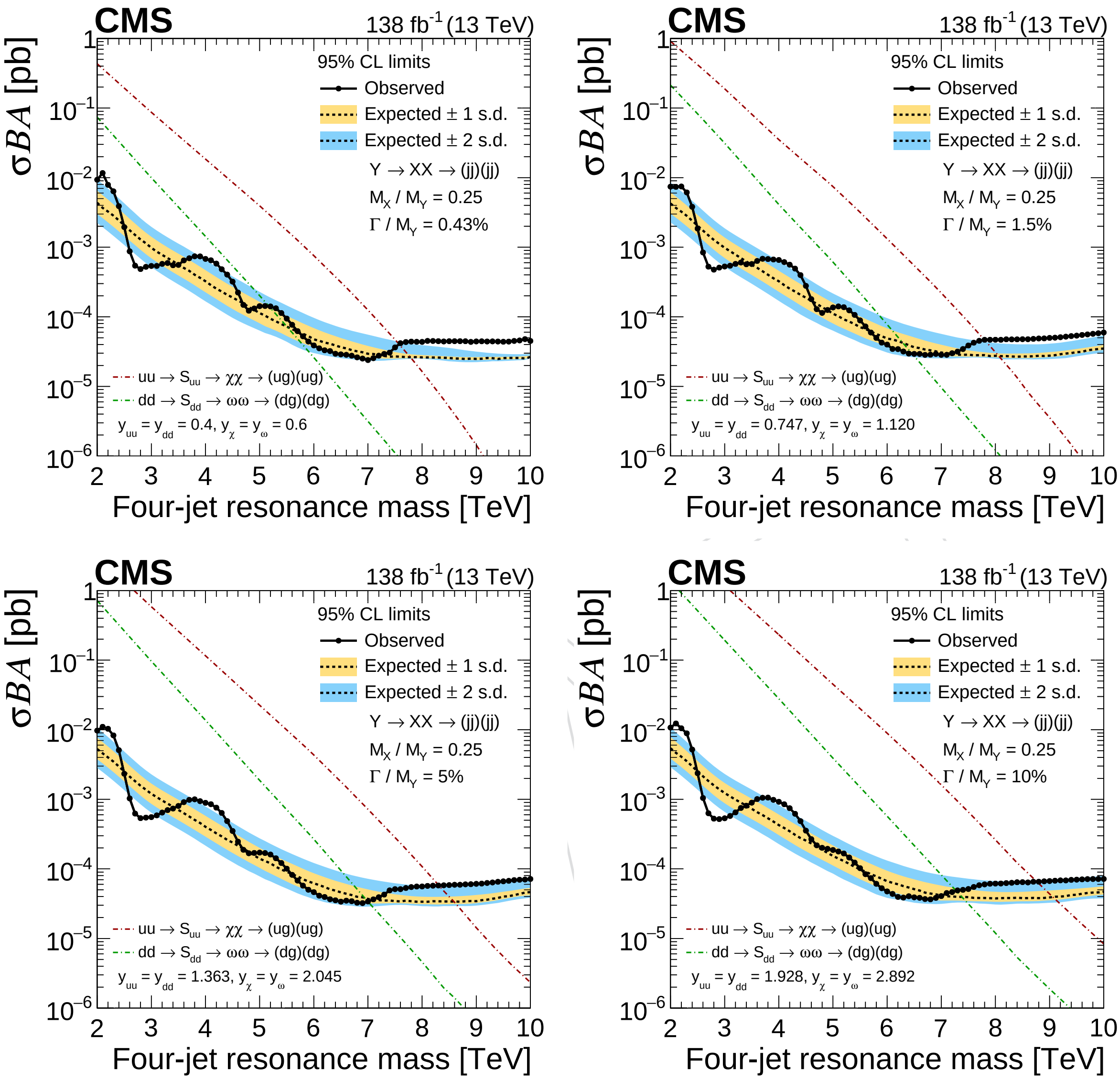

Figure 10: The observed 95% CL upper limits (points) on the product of the cross section, branching fraction, and acceptance for resonant production of paired dijet resonances, X, with $\alpha_{\text{true}} = M_X / M_Y = 0.25$ and width of initial resonance Y equal to 0.43% (top left), 1.5% (top right), 5% (bottom left) and 10% (bottom right). The corresponding expected limits (dashed) and their variations at the 1 and 2 standard deviation levels (shaded bands) are also shown. Limits are compared to predictions for scalar S_{uu} and S_{dd} diquarks [3] (dot-dashed lines) with couplings to pairs of up and down quarks, y_{uu} and y_{dd}, and to pairs of vector-like quarks, y_χ and y_ω, set appropriately in order to generate the corresponding widths.

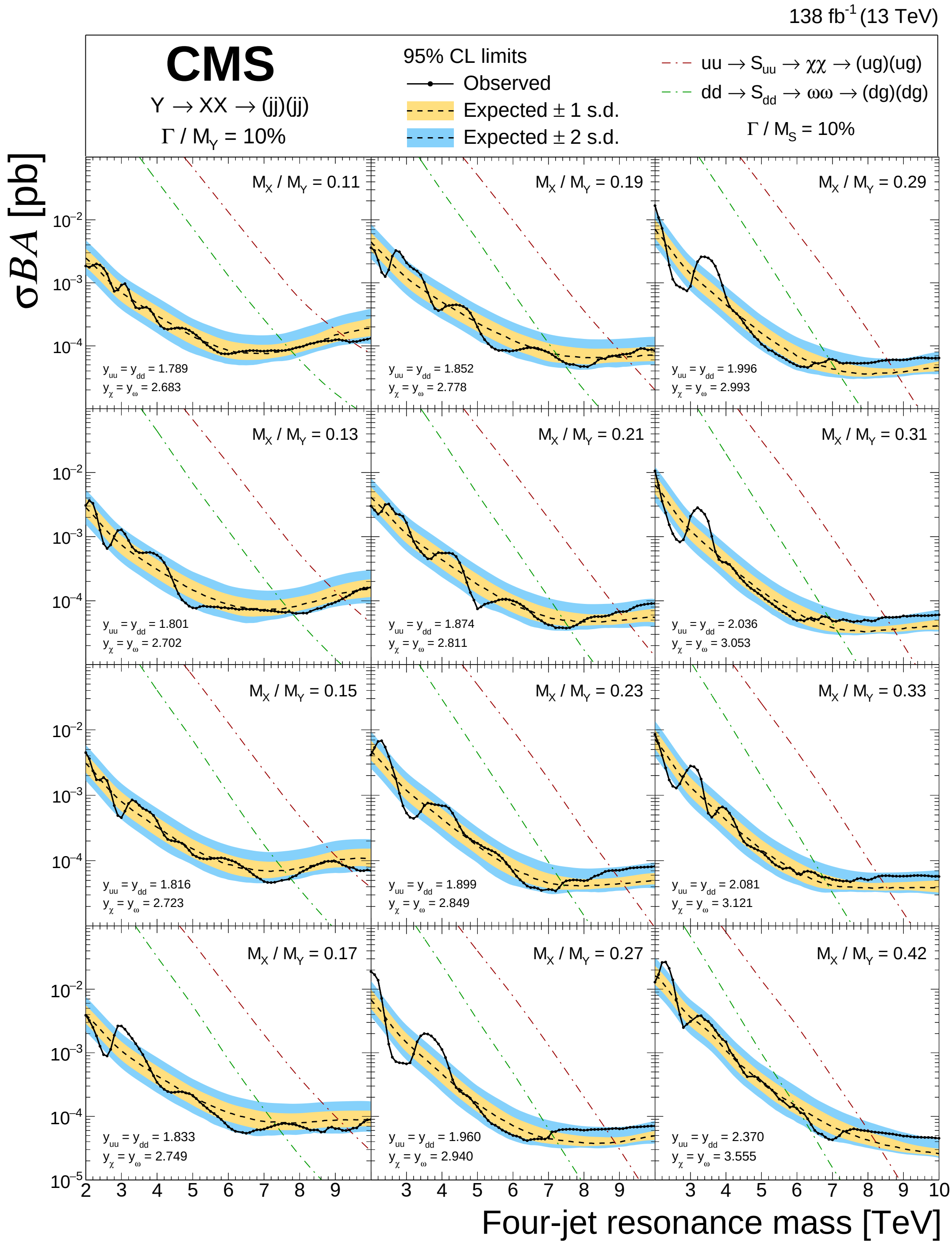

Figure 11: The observed 95% CL upper limits (points) on the product of the cross section, branching fraction, and acceptance for resonant production of paired dijet resonances, X, with width of initial resonance Y equal to 10%, and values of $\alpha_{\rm true} = M_{\rm X}/M_{\rm Y}$ shown in each panel. The corresponding expected limits (dashed) and their variations at the 1 and 2 standard deviation levels (shaded bands) are also shown. Limits are compared to predictions for scalar $\rm S_{uu}$ and $\rm S_{dd}$ diquarks [3] (dot-dashed lines) with couplings to pairs of up and down quarks, $y_{\rm uu}$ and $y_{\rm dd}$, and to pairs of vector-like quarks, y_χ and y_ω, set appropriately in order to generate a 10% width.

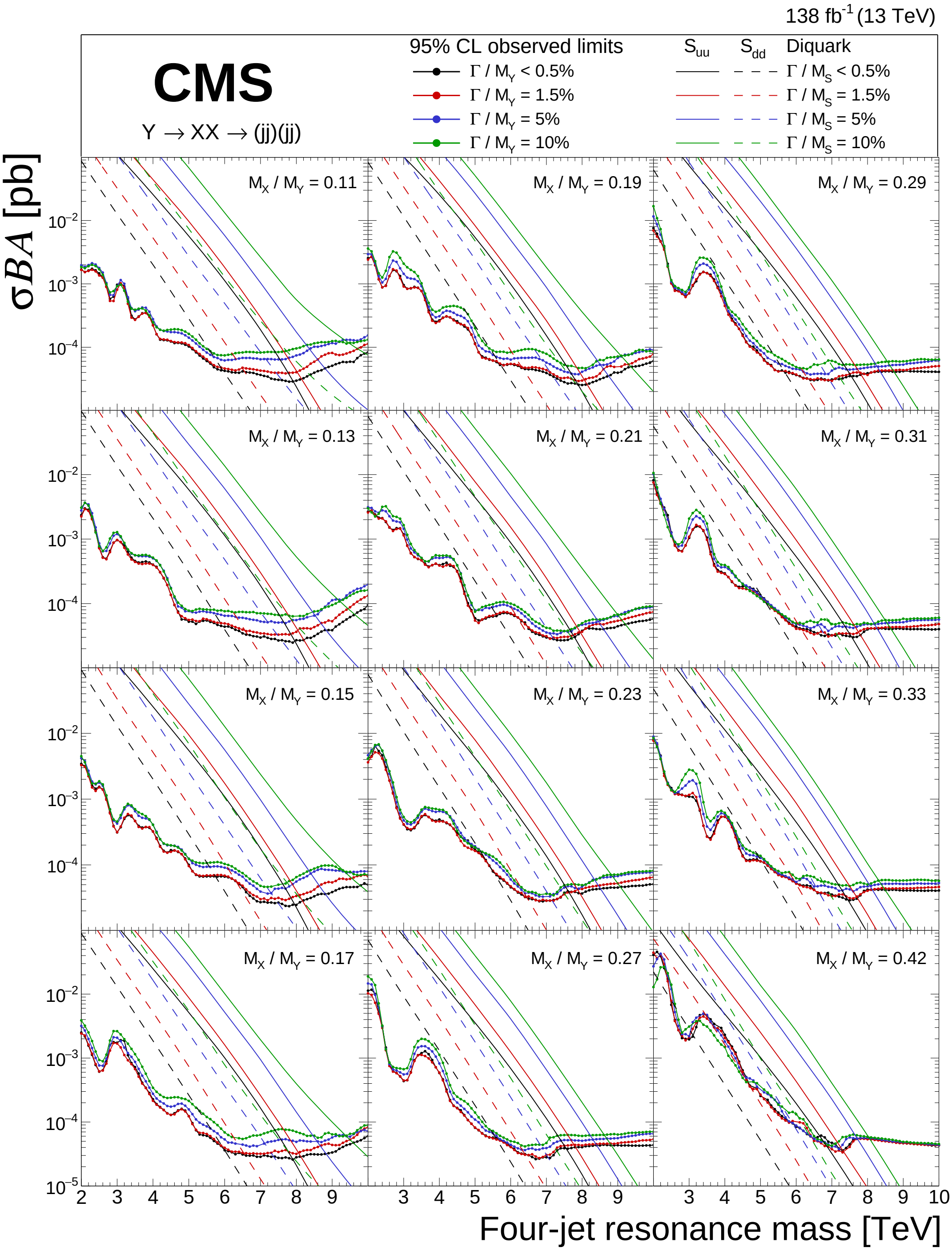

Figure 12: The observed 95% CL upper limits (points) on the product of the cross section, branching fraction, and acceptance for resonant production of paired dijet resonances, X, with the values of $\alpha_{\mathrm{true}} = M_{\mathrm{X}}/M_{\mathrm{Y}}$ shown in each panel. Different colors correspond to the various widths of the Y resonance. Limits are compared to predictions for scalar $\mathrm{S_{uu}}$ (solid lines) and $\mathrm{S_{dd}}$ (dashed lines) diquarks [3] with couplings to pairs of up and down quarks, y_{uu} and y_{dd}, and to pairs of vector-like quarks, y_{χ} and y_{ω}, set appropriately in order to generate the corresponding widths.

Table 1: Observed and expected mass limits at 95% CL for S_{uu} and S_{dd} diquark models with $\alpha_{true} = 0.25$.

Width	S_{uu} scalar diquark Observed (expected) mass limit [TeV]	S_{dd} scalar diquark Observed (expected) mass limit [TeV]
$\Gamma/M_S = 0.43\%$	7.6 (7.8)	5.2 (5.5)
$\Gamma/M_S = 1.5\%$	7.8 (8.1)	6.5 (6.3)
$\Gamma/M_S = 5\%$	8.3 (8.6)	7.0 (6.9)
$\Gamma/M_S = 10\%$	8.8 (9.1)	7.3 (7.4)

obtained without the correction. For a given model, new particles are excluded at 95% CL in mass regions where the theoretical prediction lies at or above the observed upper limit for the appropriate final state in Figs. 10–12. The exclusion mass limits, derived from Fig. 10, for S_{uu} and S_{dd} signals with $\alpha_{true} = 0.25$ are presented in Table 1. Note in Table 1 that for the 8.6 TeV resonance with a width of 10%, while the benchmark S_{uu} diquark model is excluded, the S_{dd} diquark model is not excluded and remains a viable hypothesis for our three candidate events.

In the upper plot of Fig. 13 we present the local p-value as a function of four-jet resonance mass and width, assuming $\alpha_{true} = 0.25$. The most significant signal hypothesis for a narrow resonance, as was demonstrated in Ref. [1], occurs at a four-jet resonance mass of 8.6 TeV and a dijet resonance mass of 2.15 TeV, for which the local significance is 3.9 s.d. As the four-jet resonance becomes broader, Fig. 13 demonstrates that the local significance remains high, exceeding or being equal to 3.6 s.d., even for the largest width of 10%. Hence, the significance of an 8.6 TeV diquark is found to be relatively insensitive to the choice of width, making a broad resonance an equally valid interpretation of the excess. For the look-elsewhere-effect (LEE), a large number of possible signals in the 2D plane of four-jet resonance mass and α_{true} is considered, resulting in a global significance of 1.6 s.d. for narrow and 1.4 s.d. for the broadest resonance considered.

For the previously mentioned four-jet resonance mass of 8.6 TeV with $\alpha_{true} = 0.25$ the best fit values of $\sigma\mathcal{B}A$, as well as the local and global significance results, are listed in Table 2 for each considered width, and confirm that broader resonances with widths of 5% and 10% provide a better fit for all three observed candidate events.

The entire 2D plane of four-jet resonance mass and α_{true} is furthermore scanned and a second excess is observed at four-jet resonance mass of 3.6 TeV, $\alpha_{true} = 0.29$ and 10% width with a local and global significance of 3.9 s.d. and 2.2 s.d. respectively, as shown in the lower plot of Fig. 13. This excess points to a structure in data, apparent in the three α bins of Fig. 8, that was also reported by the search for nonresonant production of pairs of dijet resonances in Ref. [1], and further discussed in Ref. [50]. Its corresponding best fit values of $\sigma\mathcal{B}A$ and significance results are presented in Table 3.

DRAFT

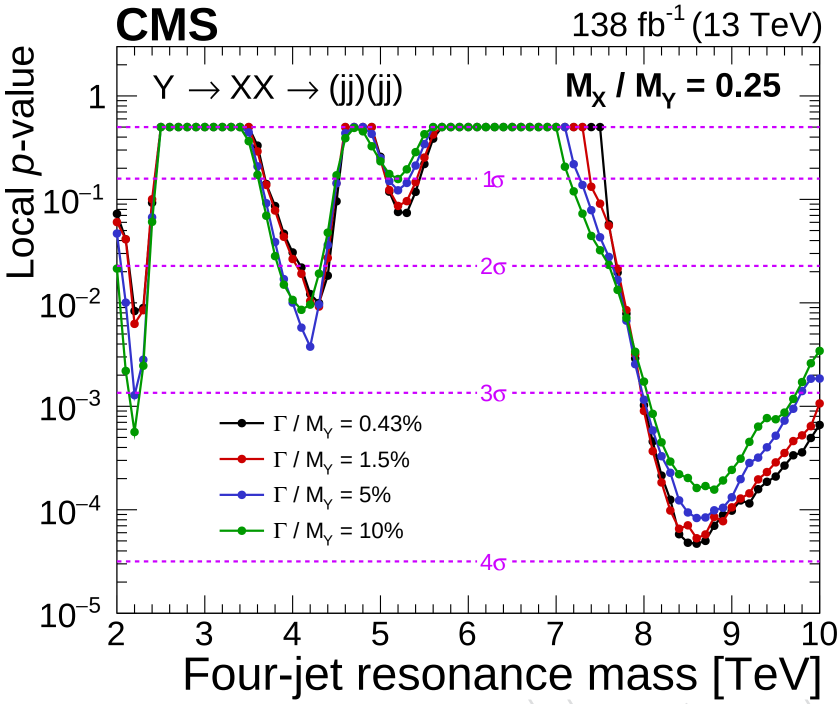

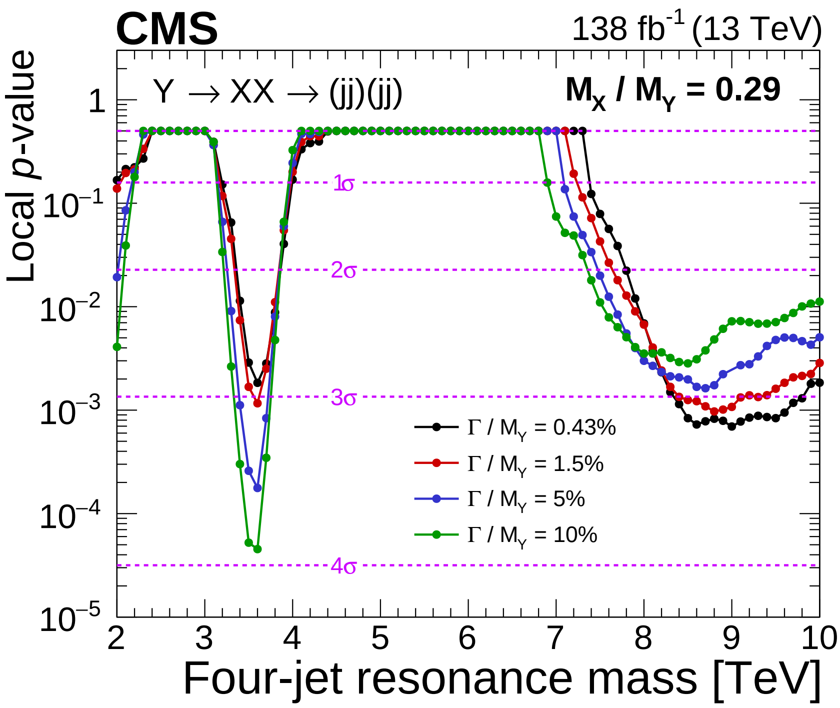

Figure 13: Observed local p-value for a four-jet resonance, Y, decaying to a pair of dijet resonances, X, with $\alpha_{\text{true}} = M_X/M_Y = 0.25$ (top) and 0.29 (bottom), and various widths of Y superimposed. Also shown are corresponding levels of local significance (dashed lines) in units of standard deviation (σ).

Table 2: Best fit values of $\sigma\mathcal{B}A$ and their corresponding values in terms of number of signal events, as well as local and global significance values, for a Y resonance mass of 8.6 TeV, X resonance mass of 2.15 TeV and different Y width scenarios.

Width	Best fit value [pb]	Best fit value [events]	Local (global) significance [s.d.]
$\Gamma / M_{\mathrm{Y}} = 0.43\%$	$1.56^{+1.42}_{-0.87} \times 10^{-5}$	$2.1^{+2.0}_{-1.2}$	3.9 (1.6)
$\Gamma / M_{\mathrm{Y}} = 1.5\%$	$1.68^{+1.50}_{-0.94} \times 10^{-5}$	$2.3^{+2.1}_{-1.3}$	3.9 (1.6)
$\Gamma / M_{\mathrm{Y}} = 5\%$	$2.04^{+1.83}_{-1.15} \times 10^{-5}$	$2.8^{+2.5}_{-1.6}$	3.8 (1.5)
$\Gamma / M_{\mathrm{Y}} = 10\%$	$2.22^{+1.99}_{-1.26} \times 10^{-5}$	$3.1^{+2.7}_{-1.7}$	3.6 (1.4)

DRAFT

Table 3: Best fit values of $\sigma\mathcal{B}A$ and their corresponding values in terms of number of signal events, as well as local and global significance values, for a Y resonance mass of 3.6 TeV, X resonance mass of 1.0 TeV and different Y width scenarios.

Width	Best fit value [pb]	Best fit value [events]	Local (global) significance [s.d.]
$\Gamma / M_{\mathrm{Y}} = 0.43\%$	$0.76^{+0.41}_{-0.29} \times 10^{-3}$	105^{+57}_{-40}	2.9 (0.1)
$\Gamma / M_{\mathrm{Y}} = 1.5\%$	$0.83^{+0.30}_{-0.32} \times 10^{-3}$	114^{+42}_{-44}	3.0 (0.5)
$\Gamma / M_{\mathrm{Y}} = 5\%$	$1.18^{+0.36}_{-0.33} \times 10^{-3}$	162^{+50}_{-46}	3.6 (1.6)
$\Gamma / M_{\mathrm{Y}} = 10\%$	$1.53^{+0.42}_{-0.40} \times 10^{-3}$	210^{+58}_{-54}	3.9 (2.2)

9 Candidate event

The high significance of narrow resonances at 8.6 TeV is predominantly caused by the two events with a four-jet mass of 8 TeV and an average dijet mass of 2 TeV, shown in Fig. 3. Although similarly isolated from the bulk of the two dimensional mass distribution, the third event, with a four-jet mass of 5.8 TeV and an average dijet mass of 2.0 TeV, has minimal contribution in the fit with narrow resonances. However, as Fig. 3 and Table 2 indicate, it is notably more compatible with broad resonances.

The three-dimensional display of this event is shown in Fig. 14. It exhibits a very similar topology and characteristics as the two events with a four-jet mass of 8 TeV, that were shown in Ref. [1]. It was collected during 2018, and has a four-jet mass of 5.8 TeV, while the invariant mass of the first dijet pair that includes jets 1 and 4 is 2.0 TeV, and the mass of the second pair from jets 2 and 3 is 1.9 TeV. The two dijet pairs are back-to-back in azimuthal angle ($|\Delta\phi| = 3.1$), nearby in pseudorapidity ($|\Delta\eta| = 0.7$), and have a mass asymmetry of 0.03. Both ΔR_1 and ΔR_2 values between the two jets in the two dijet pairs are 1.8. The p_{T}, η, and ϕ of each jet can be seen in Fig. 14.

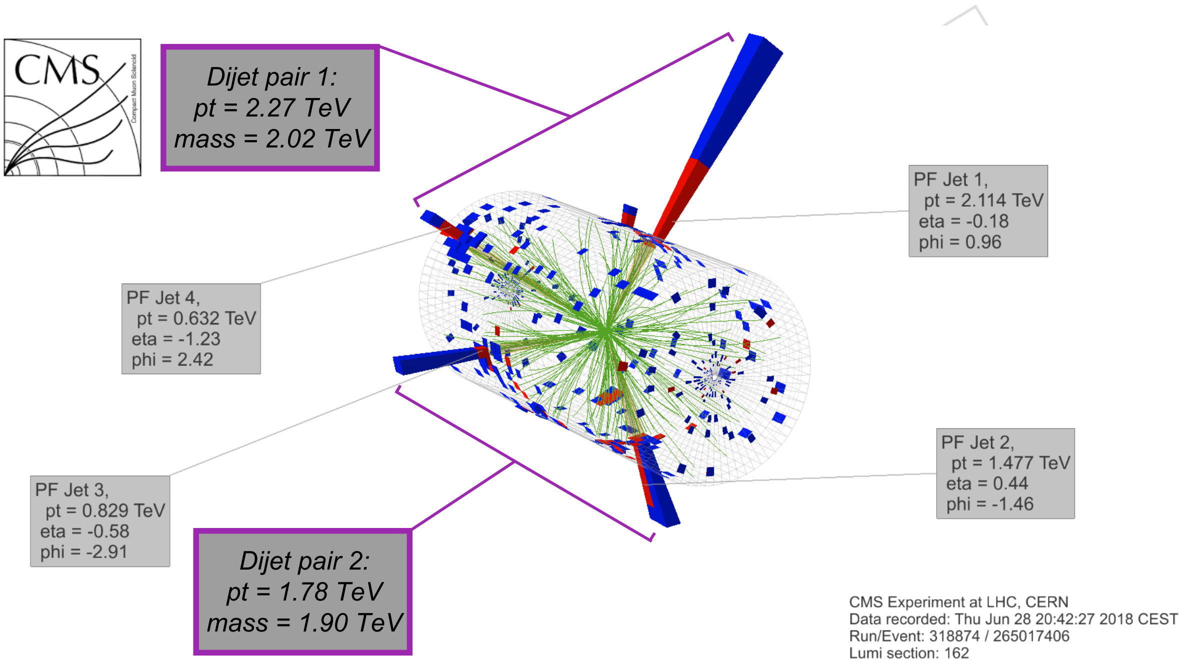

Figure 14: Three-dimensional display of the candidate event for broad resonances with a four-jet mass of 5.8 TeV. The display shows the energy deposited in the electromagnetic (red) and hadronic (blue) calorimeters and the reconstructed tracks of charged particles (green). The grouping of the four observed jets into two dijet pairs (purple boxes) is discussed in the text.

10 Summary

A reinterpretation of a narrow resonance analysis, described in Ref. [1], has been conducted and presented, searching here for resonant production of pairs of dijet resonances with the same mass through broad mediators, in final states with at least four jets. Data from proton-proton collisions at $\sqrt{s} = 13$ TeV were used in this search, collected by the CMS experiment at the LHC, corresponding to an integrated luminosity of 138 fb^{-1}.

The pairs of dijet resonances are produced via a massive broad mediator, leading to a four-jet resonance in the final state. Empirical functions that model the background, and simulated shapes of resonance signals with widths of 1.5%, 5% and 10%, are fit to the observed four-jet mass distributions in bins of the ratio of the dijet to the four-jet distributions. There are three events in the tails of the distributions, two with a four-jet mass of 8 TeV and one with a four-jet mass of 5.8 TeV, all of which have an average dijet mass of approximately 2 TeV, that result in an excess. Although the event with a four-jet mass of 5.8 TeV contributes minimally to a fit with narrow resonances, it is far more compatible with broad resonances of the same mass. Hence, the local significance for a diquark remains above 3.6 s.d. even for the largest width considered, leading to the conclusion that broad resonances are an equally valid interpretation of the excess. The ATLAS event, with a four-jet resonance mass of 6.6 TeV and an average dijet resonance mass of 2.2 TeV, falls within the CMS 68% probability contour for a 5% or a 10% wide resonance with a mass of 8.4 TeV, and hence is likely compatible with those two hypotheses.

A second excess with a local significance of 3.9 s.d. is observed at four-jet resonance mass of 3.6 TeV and average dijet resonance mass of 1.0 TeV, for a mediator width of 10%. This excess was previously reported with a local significance of 3.6 s.d. in Ref. [1], originating from the dijet data near a mass of 1 TeV, in the search for nonresonant production of pairs of dijet resonances.

Model-independent upper limits at 95% CL are presented on the product of the cross section, branching fraction and acceptance as a function of the four-jet resonance mass between 2 and 10 TeV, for all accessible values of the ratio of the dijet to four-jet resonance masses and for widths ranging from 1.5% to 10%. Limits are compared to models [3] of diquarks, which decay to pairs of vector-like quarks, which in-turn decay to a quark and a gluon. Mass limits for all accessible values of the ratio of the vector-like quark to diquark masses, and diquark widths are presented.

DRAFT

References

[1] CMS Collaboration, “Search for resonant and nonresonant production of pairs of dijet resonances in proton-proton collisions at $\sqrt{s} = 13$ TeV”, *JHEP* **07** (2023) 161, doi:10.1007/JHEP07(2023)161, arXiv:2206.09997.

[2] ATLAS Collaboration, “Pursuit of paired dijet resonances in the Run 2 dataset with ATLAS”, *Phys. Rev. D* **108** (2023) 112005, doi:10.1103/PhysRevD.108.112005, arXiv:2307.14944.

[3] B. A. Dobrescu, R. M. Harris, and J. Isaacson, “Ultraheavy resonances at the LHC: beyond the QCD background”, 2018. arXiv:1810.09429.

[4] B. A. Dobrescu, “TeV-scale particles and LHC events with dijet pairs”, arXiv:2411.04121.

[5] B. A. Dobrescu, “LHC probes of the 10 TeV scale”, arXiv:1912.13155.

[6] CMS Collaboration, “The CMS experiment at the CERN LHC”, *JINST* **3** (2008) S08004, doi:10.1088/1748-0221/3/08/S08004.

[7] CMS Collaboration, “Event generator tunes obtained from underlying event and multiparton scattering measurements”, *Eur. Phys. J. C* **76** (2016) 155, doi:10.1140/epjc/s10052-016-3988-x, arXiv:1512.00815.

[8] P. Skands, S. Carrazza, and J. Rojo, “Tuning PYTHIA 8.1: the Monash 2013 tune”, *Eur. Phys. J. C* **74** (2014) 3024, doi:10.1140/epjc/s10052-014-3024-y, arXiv:1404.5630.

[9] NNPDF Collaboration, “Parton distributions with LHC data”, *Nucl. Phys. B* **867** (2013) 244, doi:10.1016/j.nuclphysb.2012.10.003, arXiv:1207.1303.

[10] J. Alwall et al., “The automated computation of tree-level and next-to-leading order differential cross sections, and their matching to parton shower simulations”, *JHEP* **07** (2014) 079, doi:10.1007/JHEP07(2014)079, arXiv:1405.0301.

[11] T. Sjöstrand et al., “An introduction to PYTHIA 8.2”, *Comput. Phys. Commun.* **191** (2015) 159, doi:10.1016/j.cpc.2015.01.024, arXiv:1410.3012.

[12] NNPDF Collaboration, “Parton distributions for the LHC Run II”, *JHEP* **04** (2015) 040, doi:10.1007/JHEP04(2015)040, arXiv:1410.8849.

[13] GEANT4 Collaboration, “Geant4 — a simulation toolkit”, *Nucl. Instr. Meth. A* **506** (2003) 250, doi:10.1016/S0168-9002(03)01368-8.

[14] CMS Collaboration, “Particle-flow reconstruction and global event description with the CMS detector”, *JINST* **12** (2017) P10003, doi:10.1088/1748-0221/12/10/P10003, arXiv:1706.04965.

[15] M. Cacciari and G. P. Salam, “Dispelling the N^3 myth for the k_T jet-finder”, *Phys. Lett. B* **641** (2006) 57, doi:10.1016/j.physletb.2006.08.037, arXiv:hep-ph/0512210.

[16] M. Cacciari, G. P. Salam, and G. Soyez, “The anti-k_T jet clustering algorithm”, *JHEP* **04** (2008) 063, doi:10.1088/1126-6708/2008/04/063, arXiv:0802.1189.

DRAFT

[17] M. Cacciari, G. P. Salam, and G. Soyez, “FastJet user manual”, *Eur. Phys. J. C* **72** (2012) 1896, doi:10.1140/epjc/s10052-012-1896-2, arXiv:1111.6097.

[18] D. Contardo et al., “Technical Proposal for the Phase-II Upgrade of the CMS Detector”, technical report, Geneva, 2015. doi:10.17181/CERN.VU8I.D59J.

[19] CMS Collaboration, “Pileup mitigation at CMS in 13 TeV data”, *Journal of Instrumentation* **15** (2020), no. 09, P09018P09018, doi:10.1088/1748-0221/15/09/p09018, arXiv:2003.00503.

[20] CMS Collaboration, “The CMS trigger system”, *JINST* **12** (2017) P01020, doi:10.1088/1748-0221/12/01/P01020, arXiv:1609.02366.

[21] CMS Collaboration, “Performance of the CMS high-level trigger during LHC Run 2”, *JINST* **19** (2024), no. 11, P11021, doi:10.1088/1748-0221/19/11/p11021, arXiv:2410.17038.

[22] CMS Collaboration, “Jet energy scale and resolution in the CMS experiment in pp collisions at 8 TeV”, *JINST* **12** (2017) P02014, doi:10.1088/1748-0221/12/02/P02014, arXiv:1607.03663.

[23] CMS Collaboration, “Jet algorithms performance in 13 TeV data”, CMS Physics Analysis Summary CMS-PAS-JME-16-003, CERN, Geneva, 2017. https://cds.cern.ch/record/2256875.

[24] CMS Collaboration, “Search for pair-produced resonances decaying to quark pairs in proton-proton collisions at $\sqrt{s} = 13$ TeV”, *Phys. Rev. D* **98** (2018) 112014, doi:10.1103/PhysRevD.98.112014, arXiv:1808.03124.

[25] CMS Collaboration, “Search for narrow and broad dijet resonances in proton-proton collisions at $\sqrt{s} = 13$ TeV and constraints on dark matter mediators and other new particles”, *JHEP* **08** (2018) 130, doi:10.1007/JHEP08(2018)130, arXiv:1806.00843.

[26] CMS Collaboration, “Search for dijet resonances in proton-proton collisions at $\sqrt{s}$ = 13 TeV and constraints on dark matter and other models”, *Phys. Lett. B* **769** (2017) 520, doi:10.1016/j.physletb.2017.02.012, arXiv:1611.03568.

[27] CMS Collaboration, “Search for narrow resonances in dijet final states at $\sqrt{s} = 8$ TeV with the novel CMS technique of data scouting”, *Phys. Rev. Lett.* **117** (2016) 031802, doi:10.1103/PhysRevLett.117.031802, arXiv:1604.08907.

[28] CMS Collaboration, “Search for narrow resonances decaying to dijets in proton-proton collisions at $\sqrt{s} = 13$ TeV”, *Phys. Rev. Lett.* **116** (2016) 071801, doi:10.1103/PhysRevLett.116.071801, arXiv:1512.01224.

[29] CMS Collaboration, “Search for dijet resonances in 7 TeV pp collisions at CMS”, *Phys. Rev. Lett.* **105** (2010) 211801, doi:10.1103/PhysRevLett.105.211801, arXiv:1010.0203. [Erratum doi:10.1103/PhysRevLett.106.029902].

[30] CMS Collaboration, “Search for resonances in the dijet mass spectrum from 7 TeV pp collisions at CMS”, *Phys. Lett. B* **704** (2011) 123, doi:10.1016/j.physletb.2011.09.015, arXiv:1107.4771.

DRAFT

[31] CMS Collaboration, "Search for narrow resonances and quantum black holes in inclusive and b-tagged dijet mass spectra from pp collisions at $\sqrt{s} = 7$ TeV", *JHEP* **01** (2013) 013, doi:10.1007/JHEP01(2013)013, arXiv:1210.2387.

[32] CMS Collaboration, "Search for narrow resonances using the dijet mass spectrum in pp collisions at $\sqrt{s} = 8$ TeV", *Phys. Rev. D* **87** (2013) 114015, doi:10.1103/PhysRevD.87.114015, arXiv:1302.4794.

[33] CMS Collaboration, "Search for resonances and quantum black holes using dijet mass spectra in proton-proton collisions at $\sqrt{s} = 8$ TeV", *Phys. Rev. D* **91** (2015) 052009, doi:10.1103/PhysRevD.91.052009, arXiv:1501.04198.

[34] ATLAS Collaboration, "Search for new phenomena in dijet mass and angular distributions from pp collisions at $\sqrt{s} = 13$ TeV with the ATLAS detector", *Phys. Lett. B* **754** (2016) 302, doi:10.1016/j.physletb.2016.01.032, arXiv:1512.01530.

[35] ATLAS Collaboration, "Search for new particles in two-jet final states in 7 TeV proton-proton collisions with the ATLAS detector at the LHC", *Phys. Rev. Lett.* **105** (2010) 161801, doi:10.1103/PhysRevLett.105.161801, arXiv:1008.2461.

[36] ATLAS Collaboration, "Search for new physics in dijet mass and angular distributions in pp collisions at $\sqrt{s} = 7$ TeV measured with the ATLAS detector", *New J. Phys.* **13** (2011) 053044, doi:10.1088/1367-2630/13/5/053044, arXiv:1103.3864.

[37] ATLAS Collaboration, "Search for new physics in the dijet mass distribution using 1 fb^{-1} of pp collision data at $\sqrt{s} = 7$ TeV collected by the ATLAS detector", *Phys. Lett. B* **708** (2012) 37, doi:10.1016/j.physletb.2012.01.035, arXiv:1108.6311.

[38] ATLAS Collaboration, "ATLAS search for new phenomena in dijet mass and angular distributions using pp collisions at $\sqrt{s} = 7$ TeV", *JHEP* **01** (2013) 029, doi:10.1007/JHEP01(2013)029, arXiv:1210.1718.

[39] ATLAS Collaboration, "Search for new phenomena in the dijet mass distribution using pp collision data at $\sqrt{s} = 8$ TeV with the ATLAS detector", *Phys. Rev. D* **91** (2015) 052007, doi:10.1103/PhysRevD.91.052007, arXiv:1407.1376.

[40] CDF Collaboration, "Search for new particles decaying into dijets in proton-antiproton collisions at $\sqrt{s} = 1.96$ TeV", *Phys. Rev. D* **79** (2009) 112002, doi:10.1103/PhysRevD.79.112002, arXiv:0812.4036.

[41] CMS Collaboration, "Precision luminosity measurement in proton-proton collisions at $\sqrt{s} = 13$ TeV in 2015 and 2016 at CMS", *Eur. Phys. J. C* **81** (2021) 880, doi:10.1140/epjc/s10052-021-09538-2, arXiv:2104.01927.

[42] CMS Collaboration, "CMS luminosity measurements for the 2017 data-taking period", CMS Physics Analysis Summary CMS-PAS-LUM-17-004, 2018. https://cds.cern.ch/record/2621960.

[43] CMS Collaboration, "CMS luminosity measurements for the 2018 data-taking period", CMS Physics Analysis Summary CMS-PAS-LUM-18-002, 2019. https://cds.cern.ch/record/2676164.

[44] P. D. Dauncey, M. Kenzie, N. Wardle, and G. J. Davies, "Handling uncertainties in background shapes: the discrete profiling method", *JINST* **10** (2015) P04015, doi:10.1088/1748-0221/10/04/P04015, arXiv:1408.6865.

DRAFT

[45] CMS Collaboration, "The CMS statistical analysis and combination tool: Combine", *Computing and Software for Big Science* **8** (2024), no. 1, doi:10.1007/s41781-024-00121-4, arXiv:2404.06614.

[46] T. Junk, "Confidence level computation for combining searches with small statistics", *Nucl. Instr. Meth. A* **434** (1999) 435, doi:10.1016/S0168-9002(99)00498-2, arXiv:hep-ex/9902006.

[47] A. L. Read, "Presentation of search results: the CL_s technique", *J. Phys. G* **28** (2002) 2693, doi:10.1088/0954-3899/28/10/313.

[48] ATLAS and CMS Collaborations, and LHC Higgs Combination Group, "Procedure for the LHC Higgs boson search combination in summer 2011", Technical Report CMS-NOTE-2011-005, ATL-PHYS-PUB-2011-11, CERN, 2011. https://cds.cern.ch/record/1379837.

[49] G. Cowan, K. Cranmer, E. Gross, and O. Vitells, "Asymptotic formulae for likelihood-based tests of new physics", *Eur. Phys. J. C* **71** (2011) 1554, doi:10.1140/epjc/s10052-011-1554-0. [Erratum: doi:10.1140/epjc/s10052-013-2501-z].

[50] A. Crivellin, C. A. Manzari, B. Mellado, and S.-E. Dahbi, "Consistency and interpretation of the LHC dijet excesses", *Phys. Rev. D* **107** (2023), no. 5, 054045, doi:10.1103/PhysRevD.107.054045, arXiv:2208.12254.

DRAFT